Journal of Zhejiang University-SCIENCE A (Applied Physics & Engineering) 2025 26(8):707-722
www.jzus.zju.edu.cn; www.springer.com/journal/11582
E-mail: jzus_a@zju.edu.cn

Research Article

https://doi.org/10.1631/jzus.A2500007

High-performance milling of Ti-6Al-4V through rotary ultrasonic elliptical milling with anticlockwise elliptical vibration

Lianxing LIU[1,2], Xinggang JIANG[1,2], Enze YING[1,2], Zhefei SUN[1,2], Daxi GENG[1,2]✉, Deyuan ZHANG[1,2]✉

[1] *School of Mechanical Engineering and Automation, Beihang University, Beijing 100191, China*
[2] *Institute of Bionic and Micro-Nano Systems, Beihang University, Beijing 100191, China*

Abstract: Ultrasonic elliptical vibration cutting (UEVC) with clockwise elliptical vibration has made notable achievements in precision machining; however, its critical cutting speed limits its application to low-speed machining tasks. Meanwhile, rotary ultrasonic elliptical machining (RUEM) with clockwise elliptical vibration has been validated as an effective high-speed cutting technology. Unfortunately, conventional RUEM leads to increased surface roughness. To address this issue and enhance machining quality, we propose a novel RUEM method employing an anticlockwise vibration direction, called anticlockwise rotary ultrasonic elliptical machining (ARUEM). The mechanisms of surface formation and subsurface strengthening for ARUEM are analyzed. Experimental validations were performed on Ti-6Al-4V alloy, revealing that ARUEM achieved substantially lower ridge heights and up to a 50% reduction in surface roughness compared to conventional RUEM. Additionally, relative to conventional milling, ARUEM resulted in up to 122.6% thicker plastic deformation layers, 53.4% higher surface residual compressive stress, and 19.3% greater surface micro-hardness. This study showcases a promising method for high-performance milling of Ti-6Al-4V, offers new insights into RUEM by examining the influence of vibration direction, and enhances understanding of surface formation and subsurface strengthening in the ARUEM method.

Key words: Ultrasonic elliptical vibration cutting (UEVC); Vibration direction; Rotary ultrasonic elliptical machining (RUEM); Surface formation mechanism; Surface integrity; High-speed milling

1 Introduction

Ultrasonic elliptical vibration cutting (UEVC) (Moriwaki and Shamoto, 1995; Shamoto and Moriwaki, 1999; Jiang et al., 2020; Pang et al., 2021) has gained considerable attention in both research and industry (Zhang JG et al., 2016; Zhang YM et al., 2023), finding widespread application in the precision manufacturing sector (Niu et al., 2017; Wu et al., 2019). Unlike conventional one-dimensional (1D) vibration cutting, UEVC incorporates two vibration directions: one in the cutting speed direction, and one in the cutting depth direction. This dual vibration mechanism effectively reduces cutting forces, extends tool life, and improves formation accuracy and surface finish (Hu et al., 2024). As shown in Fig. 1a, all existing UEVC research has utilized clockwise elliptical vibration (Ma et al., 2004; Xiao et al., 2006). Using anticlockwise elliptical vibration in UEVC poses challenges, such as the tool flank face coming into direct contact with the workpiece and disrupting chip formation and evacuation.

Clockwise elliptical vibration facilitates intermittent cutting by the tool (Jiao et al., 2023), allowing a significant reduction in cutting force and timely entry of coolant into the cutting zone for lubrication and cooling. In addition to these benefits, it introduces several key features such as "reverse friction", "variable cutting angle", and "variable cutting speed", which can further enhance results (Ma et al., 2004). Nevertheless, the positive effect of UEVC lessens when the cutting speed exceeds the critical cutting speed, which is close to the value of the ultrasonic vibration speed (Brehl and Dow, 2008; Yang et al., 2020). As a result, UEVC is less suitable for applications requiring high processing efficiency, primarily limiting its use to precision cutting tasks.

✉ Daxi GENG, gengdx@buaa.edu.cn
Deyuan ZHANG, zhangdy@buaa.edu.cn

Lianxing LIU, https://orcid.org/0009-0003-2848-4465
Daxi GENG, https://orcid.org/0000-0003-3591-4630

Received Jan. 7, 2025; Revision accepted Apr. 8, 2025;
Crosschecked May 21, 2025; Online first June 21, 2025

To achieve intermittent cutting at high cutting speeds, Sui et al. (2017) proposed a novel ultrasonic cutting method. This approach realizes intermittent cutting through the intersection of cutting trajectories from the tool's front and rear edges, as shown in Fig. 1b. Liu et al. (2019a, 2019b) developed the method of rotary ultrasonic elliptical machining (RUEM) based on the same intermittent cutting principle, which also employs clockwise elliptical vibration and was validated through high-speed ultrasonic milling of titanium alloys. For RUEM, it was found that in comparison to conventional cutting, surface residual compressive stress and subsurface strengthening layer thickness could be increased substantially at a cutting speed of 120 m/min, and tool life could be extended by a factor of 6.4. Liu et al. (2023) further demonstrated that RUEM strengthens cutting surfaces and enhances fatigue performance. Moreover, the high-frequency periodic separation in RUEM may help suppress regenerative chatter and improve cutting stability (Sun et al., 2022; Zhang et al., 2023). Despite its advantages in achieving intermittent cutting and reducing forces at high speeds, RUEM inevitably causes residual ridges because of normal vibration in the cutting depth direction. These ridges increase surface roughness (Liu et al., 2019a, 2019b), which may negatively affect fatigue performance (Ma et al., 2018; Stopka et al., 2021). Unlike the reciprocating trajectory in UEVC, the cutting-edge trajectory in RUEM resembles overlapping sinusoidal waves, making anticlockwise elliptical vibration feasible. Utilizing anticlockwise elliptical vibration in RUEM could result in gentler residual ridges, potentially reducing surface roughness. Thus, investigating the surface formation mechanism of RUEM with anticlockwise elliptical vibration and understanding the resulting influence on surface integrity are essential for developing this machining approach.

This study aims to investigate the mechanism of surface formation and subsurface strengthening in RUEM with an anticlockwise vibration direction (referred to as anticlockwise rotary ultrasonic elliptical machining (ARUEM)), to address the issue of high surface roughness associated with conventional clockwise rotary ultrasonic elliptical machining (CRUEM). Ti-6Al-4V alloy (Sharma et al., 2009; Ulutan and Ozel, 2011), a complex material widely used in aviation manufacturing (Cellier et al., 2014; Wang and Liu, 2018), was selected to validate the feasibility of this novel elliptical vibration milling method.

The effects of the cutting process on surface topography and its mechanism were studied through evaluations of surface roughness and 2D and 3D surface topography. Additionally, the impact on mechanical properties was assessed by examining the surface residual stress, depth of the subsurface plastic deformation layer, and micro-hardness. This study aims to highlight the effectiveness of ARUEM in improving surface topography and reducing surface roughness as compared to CRUEM. In this way, the process capabilities and application scope of RUEM can be expanded for difficult-to-cut materials.

2 Kinematic analysis

2.1 Kinematic analysis of ARUEM

Side milling with a four-tooth spiral end mill is illustrated in Fig. 2a, along with a vertical view in Fig. 2b, in which the down-milling method is employed. A 2D vibration, composed of two 1D vibrations of equal amplitude, was applied on a plane perpendicular to the axis of the end mill. These 1D vibrations are perpendicular to each other and have a phase difference of 90°, thereby forming an elliptical trajectory. The

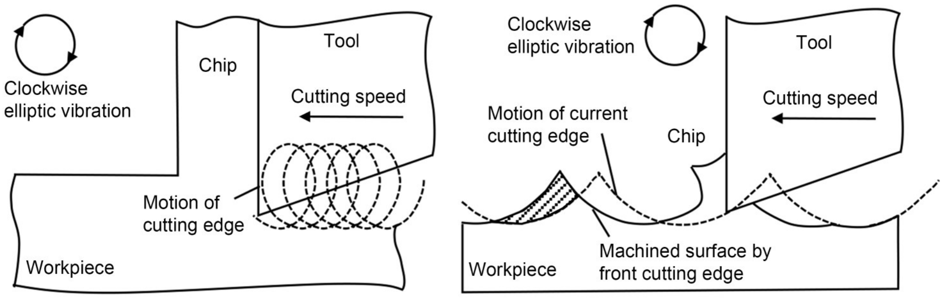

(a) (b)

Fig. 1 Schematic of (a) UEVC and (b) high-speed ultrasonic cutting

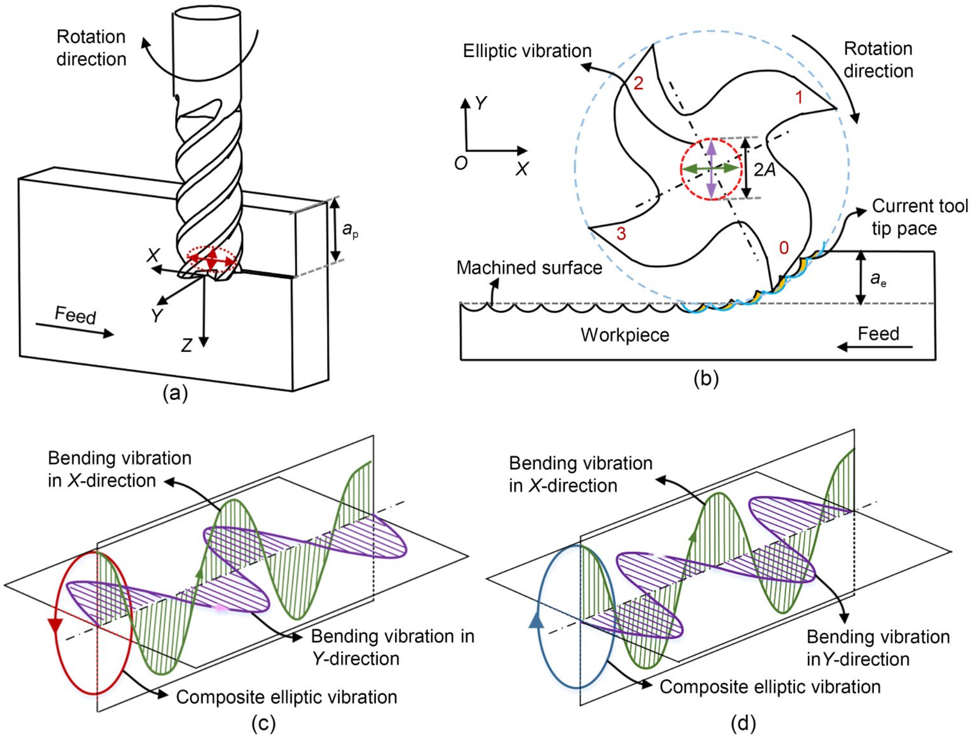

Fig. 2 Schematic view of RUEM in different elliptical vibration directions: (a) 3D view; (b) 2D view; (c) vibration direction in ARUEM; (d) vibration direction in CRUEM. a_p is the axial depth of cut; a_e is the radial depth of cut; A is the vibration amplitude of the tool tips

direction of the elliptical vibration was determined by the positive or negative phase difference. In ARUEM, the vibration direction is opposite to the tool's rotational direction, as shown in Fig. 2c. Conversely, in CRUEM, the vibration direction aligns with the tool's rotational direction, as depicted in Fig. 2d. A planar *XOY* coordinate system is established, with the initial position of the center of the end mill cutter serving as the origin, as illustrated in Fig. 2b. The feed motion occurs in the *X*-direction.

For our purposes, the theoretical motion trajectory in the superficial layer in ARUEM and CRUEM can be simplified to a forward fluctuation in the *X*-direction (Liu et al., 2019a), because the surface integrity of the machined surface is the focus of this study. Complete details of these derivations are provided in Section S1 of the electronic supplementary materials (ESM).

The simplified theoretical trajectory of one tool tip in ARUEM can be determined as:

$$\begin{cases} x_{\text{ARUEM}} = -\dfrac{2\pi nr}{60}t - A\sin(2\pi ft), \\ y_{\text{ARUEM}} = A\cos(2\pi ft), \end{cases} \tag{1}$$

where x_{ARUEM} is the displacement in the *X*-direction in ARUEM; y_{ARUEM} is the displacement in the *Y*-direction in ARUEM; n is the spindle speed; r is the radius of the end mill; t is the cutting time; f is the vibration frequency.

While for CRUEM it can be determined as:

$$\begin{cases} x_{\text{CRUEM}} = -\dfrac{2\pi nr}{60}t + A\sin(2\pi ft), \\ y_{\text{CRUEM}} = A\cos(2\pi ft). \end{cases} \tag{2}$$

Simplified theoretical movement trajectories of a singular tool tip near the final surface in ARUEM and CRUEM for varying parameters are shown in Fig. 3. The theoretical motion trajectories of the ARUEM and CRUEM reverse direction in *X*-direction when the maximum vibration speed exceeds the linear speed of the cutting-edge rotation.

The relationship between the resultant cutting speed and cutting trajectory in ARUEM and CRUEM is addressed in Section S2 of the ESM. ARUEM and CRUEM exhibit differing speed variation characteristics during different stages of cutting.

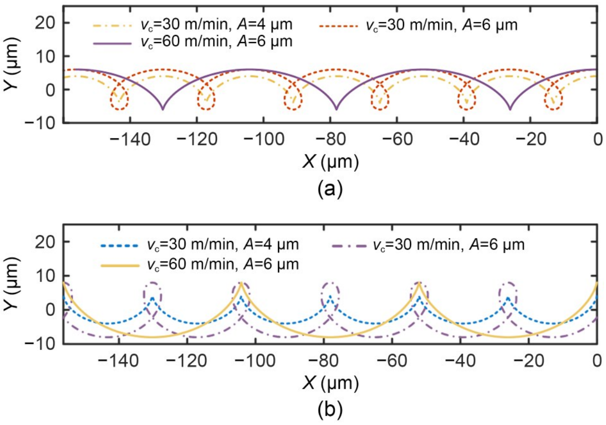

Fig. 3 Simplified movement trajectory in (a) ARUEM and (b) CRUEM at the workpiece feed rate per tooth of f_z= 0.015 mm/z. v_c is the milling speed

An analysis of acceleration is presented in Section S3, where the negative Y-direction acceleration is related to the instantaneous impact force of the cutting edge. It was found that ARUEM shows a higher proportion of trajectory points where the Y-direction acceleration is negative, suggesting stronger cutting ability in this direction (Sun et al., 2024). Conversely, CRUEM shows a larger negative Y-axis force during the cutting-in phase, which contributes to the ironing effect on the tool flank.

2.2 Surface formation and strengthening mechanism in ARUEM

The two simplified trajectory equations (Eqs. (1) and (2)) represent the path of motion for a single tool tip in the free state. However, to accurately describe the final surface morphology, modifications are required to account for the interaction between the cutting edges' flank face and the workpiece. Figs. 4b and 4c illustrate the ironing effect of the cutting edge on the workpiece surface microstructure for ARUEM and CRUEM, respectively. As the cutting edge follows the theoretical motion trajectory, the tool flank may compress the ridges formed by the previous cutting pass. These ridges, in turn, exert a reaction force on the cutting edge. For simplicity, changes in the material's mechanical properties due to this compression are not considered in our analysis. The vibration cutting system transmits energy to the cutting edge through a downward driving elastic force, which influences its motion. Under the action of this force, the cutting edge gradually presses downward. Because of the relatively

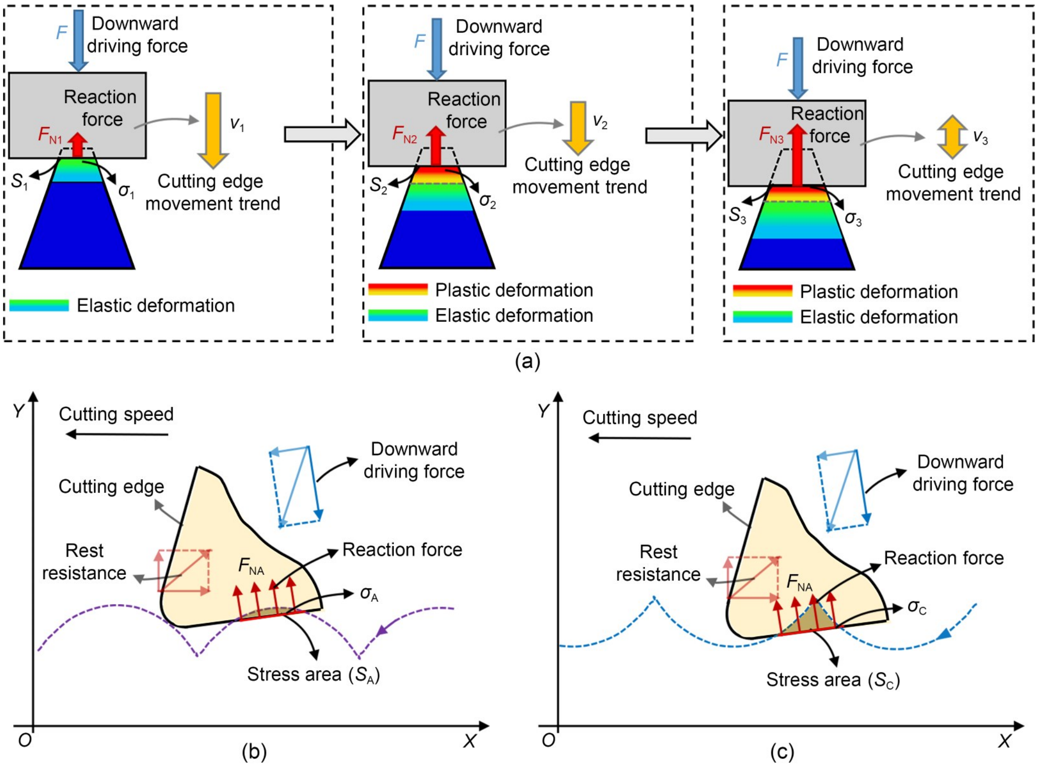

Fig. 4 Schematic of mechanical behavior (a) during ironing and stress analysis in ARUEM (b) and CRUEM (c). Subscripts A and C indicate ARUEM and CRUEM, respectively

low mass of the cutting edge, it can be assumed that the downward pressing motion quickly stops once the reaction force exceeds the downward driving force. This balance between forces determines the final trajectory and behavior of the cutting edge during machining. The formula for the reaction force is:

$$F_{\mathrm{N}}=S\sigma, \tag{3}$$

where F_{N} is the reaction force, S is the action area, and σ is the stress on the action surface. The focus of our analysis is the change in stress and action area that occurs during the pressing process.

As shown in Fig. 4a, the initial reaction force during the application of downward pressure on the tool flank is less than the downward driving force from the vibration cutting system. As the cutting edge continues being pressed down, it causes varying degrees of plastic deformation at the ridge. The stress on the surface increases until reaching its highest value (close to the material's yield strength), at which point plastic deformation occurs. As the application of downward pressure continues, the area of action gradually increases until the reaction force from the ridge on the cutting edge exceeds the downward driving force. If the action area is large enough, the pressing process may cease during the elastic deformation stage. This suggests that the sharpness of the ridge is inversely related to the depth of the depression. Therefore, the simplified trajectory equation (Eq. (2)) should describe the actual motion of the cutting edges in CRUEM, as shown in Fig. 4c; this is consistent with the views expressed in previous studies (Liu et al., 2019a, 2019b). In ARUEM, because of the associated relatively flat ridges, a large action area is generated when the cutting edge is pressed down to a small depth, resulting in a larger reaction force. When the reaction force exceeds the downward driving force acting on the cutting edge, the cutting edge will no longer be pressed down. Instead, it may move along the tool flank under the action of the driving force, as shown in Fig. 4b. Therefore, some corrections to the simplified theoretical trajectory equation for ARUEM are required to describe the true trajectory.

Based on the analysis above for ARUEM, one can assume that the position where the instantaneous working relief angle of the cutting edges is equal to zero is the initial position of the cutting edge moving along the tool flank. Moreover, when the instantaneous working relief angle of the cutting edges is greater than zero, the linear motion stops (Fig. 5).

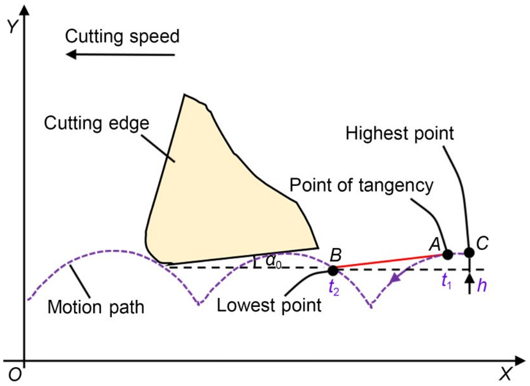

Fig. 5 Schematic of the corrected motion trajectory for ARUEM. α_0 is the nominal relief angle; h is the height of the ridge

The corrected motion trajectory for ARUEM in a vibration period can be expressed as:

$$\begin{cases} x_{\mathrm{A}}=-\dfrac{2\pi nr}{60}t-A\sin(2\pi ft), & 0\leqslant t\leqslant \dfrac{1}{f}, \\ y_{\mathrm{A}}=A\cos(2\pi ft), & 0\leqslant t\leqslant t_1,\ t_2\leqslant t\leqslant \dfrac{1}{f}, \\ y_{\mathrm{A}}=(x_{\mathrm{t2}}-x_{\mathrm{t1}})\tan\alpha_0+y_{\mathrm{t1}}, & t_1<t<t_2, \end{cases} \tag{4}$$

where x_{A} is the displacement in the X-direction of the corrected motion trajectory for ARUEM; y_{A} is the displacement in the Y-direction of the corrected motion trajectory for ARUEM; t_1 is the time when the cutting edge moves to point A; t_2 is the time when the cutting edge moves to point B; x_{t2} is the X-coordinate of point B; x_{t1} is the X-coordinate of point A; y_{t1} is the Y-coordinate of point A. The detailed derivation of the corrected motion trajectory for ARUEM is provided in Section S4.

To study the final morphology in ARUEM and CRUEM, it is necessary to investigate the envelope profile based on the trajectory of the cutting edge. The schematic of the envelope profile and the method for obtaining surface residual heights are detailed in Section S5. The theoretical residual height of one cutting edge given other parameters can be obtained using the same method illustrated in Fig. 6. The theoretical residual height in ARUEM was lower than in CRUEM for the same parameters. Additionally, the theoretical residual heights in both CRUEM and ARUEM increased with cutting speed. They also increased with respect

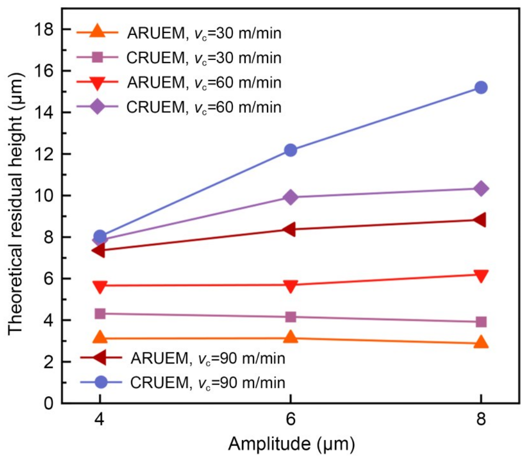

Fig. 6 Theoretical residual height of one cutting edge

to amplitude at cutting speeds within the range of 60–90 m/min, but the slopes of these trends in ARUEM were smaller than in CRUEM. When the cutting speed was 30 m/min, the theoretical residuals in CRUEM and ARUEM decreased with increasing amplitude.

Moreover, the elastic and plastic deformation caused by the ironing of the cutting edge needs to be considered to make a qualitative comparison of the residual height in ARUEM and CRUEM. Fig. 7 shows a schematic of surface topography and deformation in ARUEM and CRUEM. Because the deformation of the ridges was not accounted for in the analysis of the corrected ARUEM trajectory shown in Fig. 6, the actual formed surface should exhibit a thin and unrecoverable plastic deformation based on the theoretical envelope surface. In CRUEM, there may be some rebound at the lowest point of the cutting edge, while some sharp ridges undergo plastic deformation that cannot be restored. Therefore, considering the elastic-plastic deformation, the actual surface residual height in CRUEM should be slightly smaller than that of the envelope curve, whereas the actual residual height in ARUEM is similar to that of the envelope curve. Ultimately, the residual height in ARUEM remains smaller than in CRUEM.

In addition, it should be noted that during the cutting processes in ARUEM and CRUEM, the ironing effect of the tool flank and the impact effect of the cutting edge generate a plastic strengthening layer on the machined surface. The plastic strengthening effect in ARUEM, however, is weaker than that in CRUEM, because the plastic extrusion in CRUEM is more sufficient. Section S6 provides further analysis of the ironing processes in ARUEM and CRUEM.

3 Experimental procedure

3.1 Materials

The workpiece material used in the experiment was a Ti-6Al-4V alloy with a net basket microstructure (Fig. 8). The mechanical properties of the Ti-6Al-4V alloy are listed in Table 1. To ensure consistency in the material properties, the specimens were cut from the same piece of Ti-6Al-4V.

3.2 Experimental setup

A series of side milling tests were performed using a rotary ultrasonic vibration cutting system mounted on a three-axis vertical machining center (BV100, BMEIMT Co., Ltd., China) (Fig. 9b), which was cooled and lubricated with a water-based cutting fluid. As shown in Fig. 9a, the two core components of the rotary ultrasonic vibration cutting system are a dual ultrasonic signal generator and a dual-phase bending ultrasonic

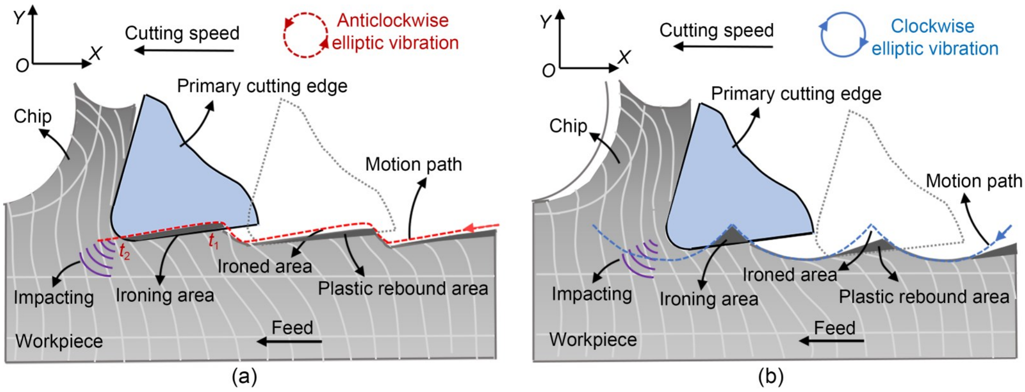

Fig. 7 Schematic of surface topography and deformation in (a) ARUEM and (b) CRUEM

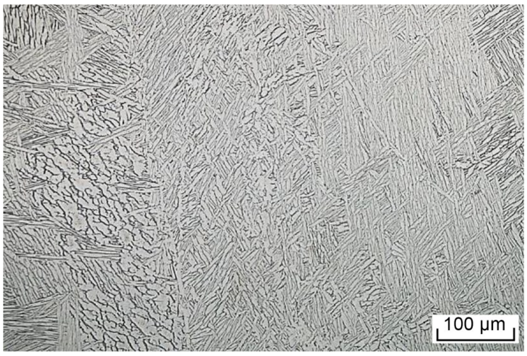

Fig. 8 Representative microscopic image of Ti-6Al-4V microstructure

Table 1 Thermo-mechanical properties of Ti-6Al-4V alloy

Parameter	Value
Density (kg/m^3)	4429
Hardness (HV)	285
Elastic modulus, E (GPa)	114
Poisson's ratio, v	0.33
Melting temperature (°C)	1677
Thermal conductivity (W/(m·K))	6.7
Yield strength (MPa)	835
Tensile strength (MPa)	905
Reduction in area (%)	34

vibration transducer. The functionality of the ultrasonic signal generator and the structure of the ultrasonic vibration transducer are detailed in Section S7. By exchanging the access relationship between the two groups of ceramic plates and the two channels of signals, the milling cutter can perform both clockwise and anticlockwise elliptical vibrations. In the experiment, the resonance frequency of the transducer was 19200 Hz.

The vibration amplitude of the milling cutter can be measured using a laser micrometer. By adjusting the power of the two signals, the bending vibration amplitudes in both directions of the milling cutter can be made equivalent, so that the coupled vibration trajectory approximates a circle. The ultrasonic signal generator displays the current value, and it was found that the current during milling was essentially the same as that in the free state. This is attributed to the frequency tracking and power feedback functions of the ultrasonic signal generator (Komatsu, 1985; Jiang et al., 2018). One can consider that the vibration amplitude measured in the free state represents the vibration level during milling.

The dual-phase ultrasonic vibration transducer was connected to the BT50 tool shank through a flange at the vibration node. A down-milling process was used in the experiment. When the elliptical rotary direction of the milling cutter aligns with the rotational direction of the milling cutter, the action is called CRUEM, and when the directions are in opposition, it is called

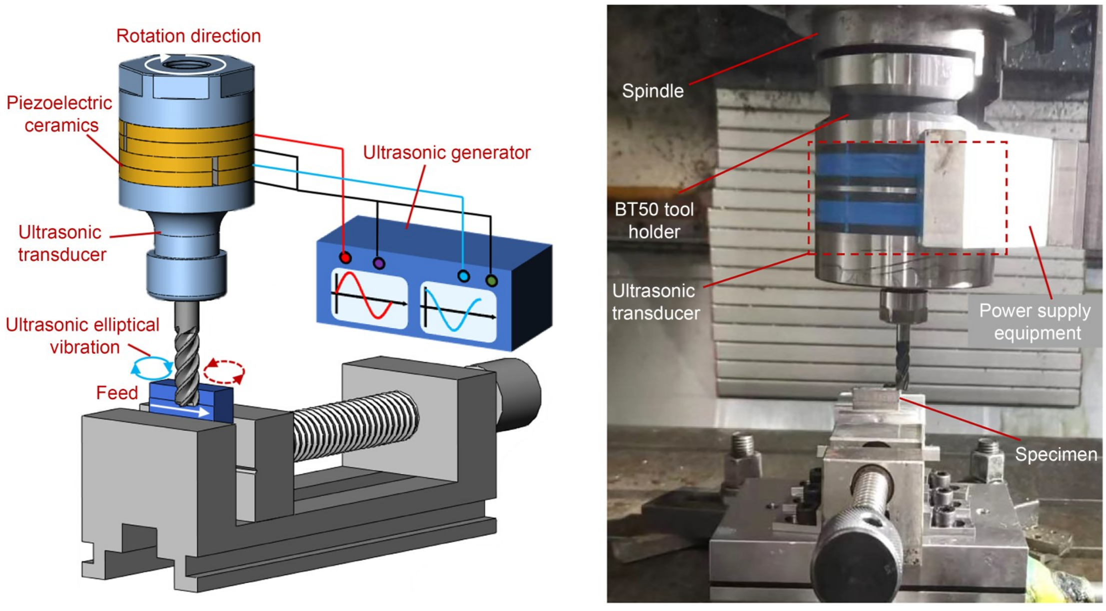

Fig. 9 Experimental setup: (a) schematic; (b) actual platform

ARUEM. Conventional machining (CM) was also performed for comparison by turning off the ultrasonic vibration power supply.

The end mill used in the experiment is the SAT S460 end mill (SAT, Japan) with a diameter of 10 mm. Its specific parameters are listed in Table 2.

Table 2 Specifications of the end mill

Tool parameter	Description
Coating	AlTiN
Spiral length (mm)	25
Number of cutting edges	4
Diameter (mm)	10
Helix angle (°)	35
Rake angle of side edge (°)	8
Relief angle of side edge (°)	10

Specimens used for surface integrity testing were cut into plates with the shape of 30 mm×26 mm×8 mm. To ensure effective measurement, 3–5 points were selected along the feed direction to measure the surface integrity parameters. In order to avoid the effect of tool wear, the end mill was replaced when the cutting parameters were changed. Cutting parameters in the test are shown in Table 3.

Table 3 Cutting parameters of CM, ARUEM, and CRUEM

Milling condition	Description
Milling speed, v_c (m/min)	30, 60, 90
Feed rate per tooth, f_z (mm/z)	0.015
Radial depth of cut, a_e (mm)	0.2
Axial depth of cut, a_p (mm)	5
Vibration amplitude, A (μm)	0, 4, 6, 8
Milling method	CM, ARUEM, CRUEM

3.3 Measurement methods

The 2D topography of the machined surface was captured using a super-depth microscope (KEYENCE VHX7000, Japan). Surface roughness was measured with a probe roughness meter (MITUTOYO SJ-410, Japan). Additionally, the 3D topography of the machined surface was assessed using a white-light interference surface topography instrument (ZYGO NexView, USA). To accurately examine the cross-sectional contour of the machined surface under varying parameters, data points parallel to the feed direction were extracted from the 3D data matrix. Residual stress in the feed direction was non-destructively measured using X-ray diffraction (XRD, Rigaku Automate II, Japan) with a light spot with a diameter of 3 mm. The surface micro-hardness was determined using a Vickers indenter (HVS-1000AT, Shanghai Kunyu Electromechanical Equipment Co., Ltd., China).

Finally, observation samples, each 6 mm in length, were cut along the feed direction using wire cutters and prepared as metallographic samples. Cross-sections of the samples were ground, polished, and then etched with a chemical reagent. After processing, the subsurface grain structure was examined using a scanning electron microscope (SEM, SIGMA500, Carl Zeiss AG, Germany).

4 Results and discussion

4.1 Surface topography and surface roughness

4.1.1 Surface topography analysis

To characterize the finished surface topography, the machined surfaces resulting from ARUEM, CRUEM, and CM were captured by an optical microscope, as shown in Fig. 10. It can be observed that the surfaces machined by ARUEM and CRUEM had reduced scratching compared to CM. Consistent with previous results, regular ridge textures are seen in the products of ARUEM and CRUEM, and the primary spacing of this ridge texture is equal to the distance traveled by the cutting edges in one vibration period (Liu et al., 2023), which is proportional to the cutting speed and independent of the vibration amplitude. As reported by Pang et al. (2021) and Chang et al. (2024) in their research on longitudinal-torsional ultrasonic milling, these regular vibration textures can suppress friction and the growth of contact nodes in the contact area. This suggests that one edge primarily performs the cutting, and the other edges play a secondary role in the surface machining.

The texture machined by the secondary edges of ARUEM was more prominent than that of CRUEM, which suggests that ARUEM has a better cutting capacity. The 3D topographies of the machined surfaces are presented in Section S8, and demonstrate that ARUEM produced flatter surfaces (with reduced ridge heights and lower undulation amplitudes) compared to CRUEM. This is consistent with our earlier analysis from Section 3, where a larger acceleration in the negative *Y*-direction when the ARUEM cutting edge engages

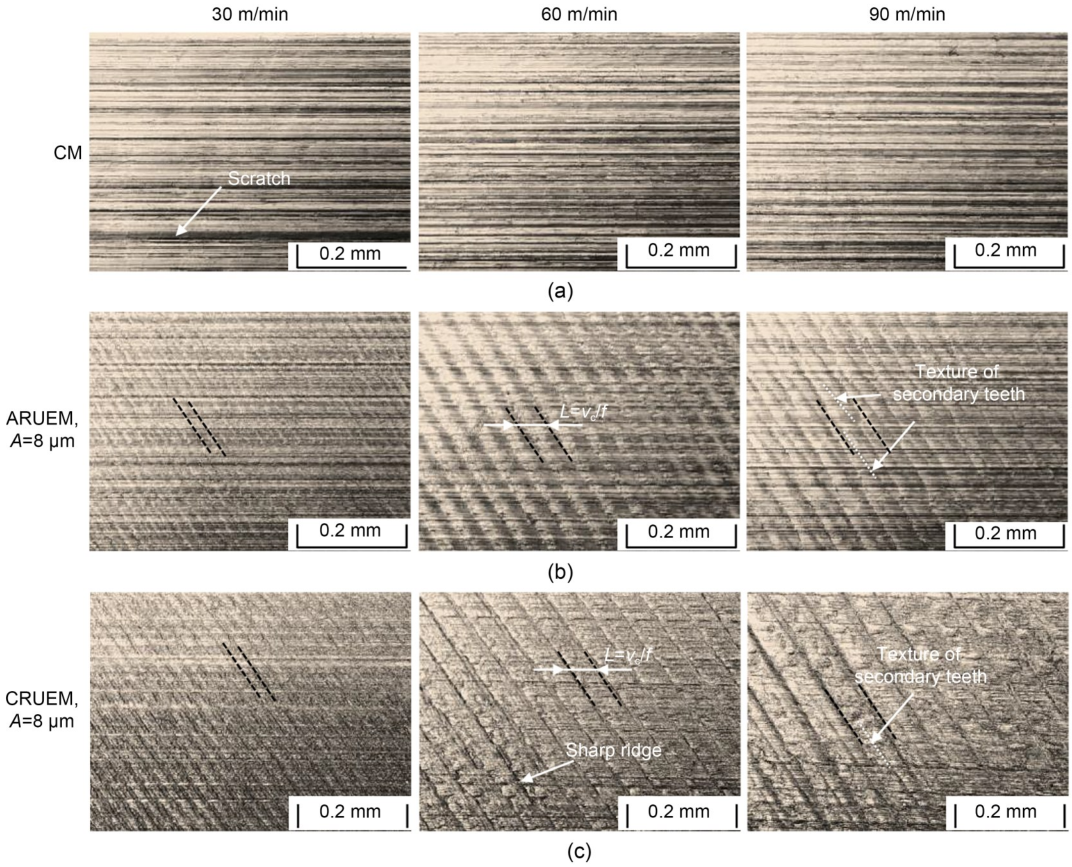

Fig. 10 Machined surface topographies under different vibration parameters for: (a) CM; (b) A=8 μm in ARUEM; (c) A=8 μm in CRUEM. L is the distance that the cutting edge moves forward in one vibration period

may lead to greater instantaneous impact forces, thus resulting in stronger normal-direction cutting capability on the workpiece surface. In addition, the surface obtained using ARUEM was smoother than that obtained using CRUEM, with more pronounced sharp ridges being observed on the CRUEM-machined surface.

A metallographic image of the section resulting from ARUEM is shown in Fig. 11, which provides an intuitive view of the surface topography and subsurface grain deformation. Because four-tooth milling cutters were used in this study, the final surface can be better represented by the four theoretical cutting envelope trajectories. Compared with the theoretical trajectory for ARUEM shown in Fig. 3, the machined surface does not exhibit sharp grooves. This indicates that during the actual cutting process, the cutting edge did not follow the exact theoretical trajectory due to the influence of the reaction force from the workpiece. As shown in Fig. 11, the envelope curve of the corrected ARUEM trajectory in Section 2.2 aligns well with the actual machined surface, demonstrating that the corrected trajectory is relatively accurate. Subsurface metallography also revealed that there was no significant fiber bending caused by the ironing effect, demonstrating the effective cutting capacity of the cutting edges in ARUEM.

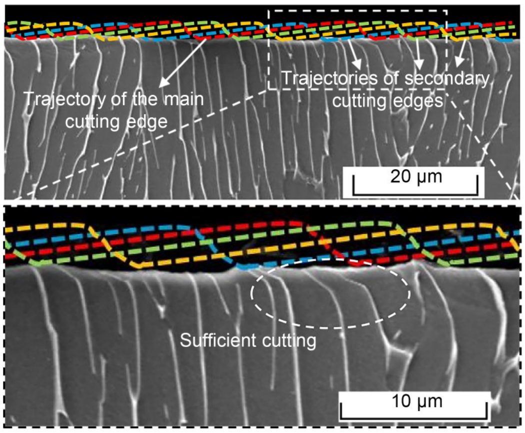

Fig. 11 Fitting diagram of the envelope locus and metallographic cross-section topography in ARUEM for v_c=30 m/min and A=4 μm

4.1.2 Surface roughness

The surface roughness (R_a) values obtained by CM, ARUEM, and CRUEM under different cutting speeds and vibration amplitudes are illustrated in Fig. 12. In keeping with previous research findings (Liu et al., 2019b), the surface roughness resulting from ARUEM and CRUEM was higher than that in CM. This can be explained by the residual heights caused by vibration cutting, which are perpendicular to the machined surface of the workpiece, thereby increasing the surface roughness (Liu et al., 2019b; Liao ZR et al., 2021).

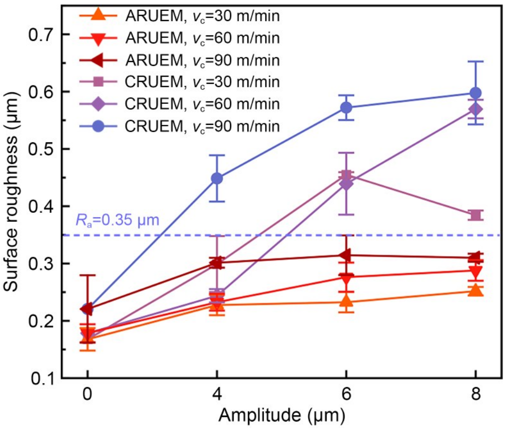

Fig. 12 Influence of elliptic vibration direction, vibration amplitude, and cutting speed on surface roughness R_a

Notably, the surface roughness R_a in ARUEM was significantly lower than in CRUEM across all machining parameters, which is consistent with the topography results of the machined surfaces shown above. When the cutting speed ranged from 30 to 90 m/min, the R_a in ARUEM was 34.5%–50.0% lower than in CRUEM for vibration amplitudes between 6 and 8 μm. Additionally, the R_a achieved by ARUEM was much lower than 0.35 μm, while in CRUEM it exceeded 0.35 μm, for vibration amplitudes in the range of 6–8 μm. This can be attributed to the lower residual height under the corrected trajectory (Fig. 6), and the stronger cutting ability of the cutting edges (Section 3).

In ARUEM, the surface roughness increased as the vibration amplitude increased, though the growth rate was relatively slow when the vibration amplitudes were 4–8 μm. This is similar to the trend of the theoretical residual height of a single cutting edge with respect to amplitude at cutting speeds ranging from 60 to 90 m/min. At a cutting speed of 30 m/min, the actual surface roughness increased slightly with vibration amplitude because the surface topography was more sensitive to cutting stability at low speeds. In CRUEM, the surface roughness increased with the vibration amplitude for most parameter configurations, and the rate of this growth was much larger than in ARUEM. This trend is also consistent with the theoretical analysis of residual height for a single cutting edge. As a result, compared to CRUEM, the rate of decrease in surface roughness for ARUEM becomes larger as the vibration amplitude increases under these conditions. However, in CRUEM, the surface roughness initially increased with increasing vibration amplitude until the vibration amplitude reached 6 μm, after which it decreased as amplitude continued to increase under a cutting speed of 30 m/min. This can be explained by the relatively small cutting unit operating at a cutting speed of 30 m/min. As reported by Liu et al. (2019b), the roughness may increase due to ploughing effects at low vibration amplitudes. Showing consistency with other experimental findings (Liu et al., 2019b), the surface roughness R_a for CM increases as the cutting speed rises from 30 to 90 m/min, since the increased cutting speed degrades the stability of the CM system. Overall, as the cutting speed increases from 30 to 90 m/min, R_a increases for both ARUEM and CRUEM, which can be attributed to the growing theoretical residual height (Fig. 6) and the degrading cutting system stability. However, in CRUEM, when the vibration amplitude was between 4 and 6 μm, the R_a at a cutting speed of 30 m/min was higher than at 60 m/min. This can be explained by the ploughing phenomenon that occurs at lower cutting speeds, where the cutting units become finer as the cutting speed decreases (Chen et al., 2021; Stopka et al., 2023).

4.2 Surface strengthening features

4.2.1 Subsurface metallographic structure

Plastic deformation is known to occur under mechanical and thermal loads during cutting (la Monaca et al., 2021; Seenath and Sarhan, 2024) and can reflect the effect of cutting strengthening (Shaikh et al., 2017; Wojciechowski et al., 2019). Yao et al. (2024) demonstrated that fibrous structures on a machined surface can enhance the fatigue performance of components. Furthermore, the surface deformation layer can increase the yield strength of the surface material and reduce the probability of dislocations forming at the surface. Cross-sectional images of the subsurfaces resulting from ARUEM, CRUEM, and CM are shown in Fig. 13. No white layers or subsurface defects such as cracks, laps, or tears were observed under the experimental conditions in our study, which is the same as Liao et al. (2019). The plastic deformation layer thickness in CM increased as the cutting speed rose from 30 to 60 m/min, then decreased when the cutting speed reached 90 m/min. This can be explained by the increase in cutting force with cutting speed within a certain range, as well as the significant rise in cutting temperature with cutting speed, which makes the material easier to cut (Liu et al., 2019b; Liao YS et al., 2021). The deformation layer thickness decreased in both ARUEM and CRUEM as the cutting speed increased. Liu et al. (2019b) showed that the cutting

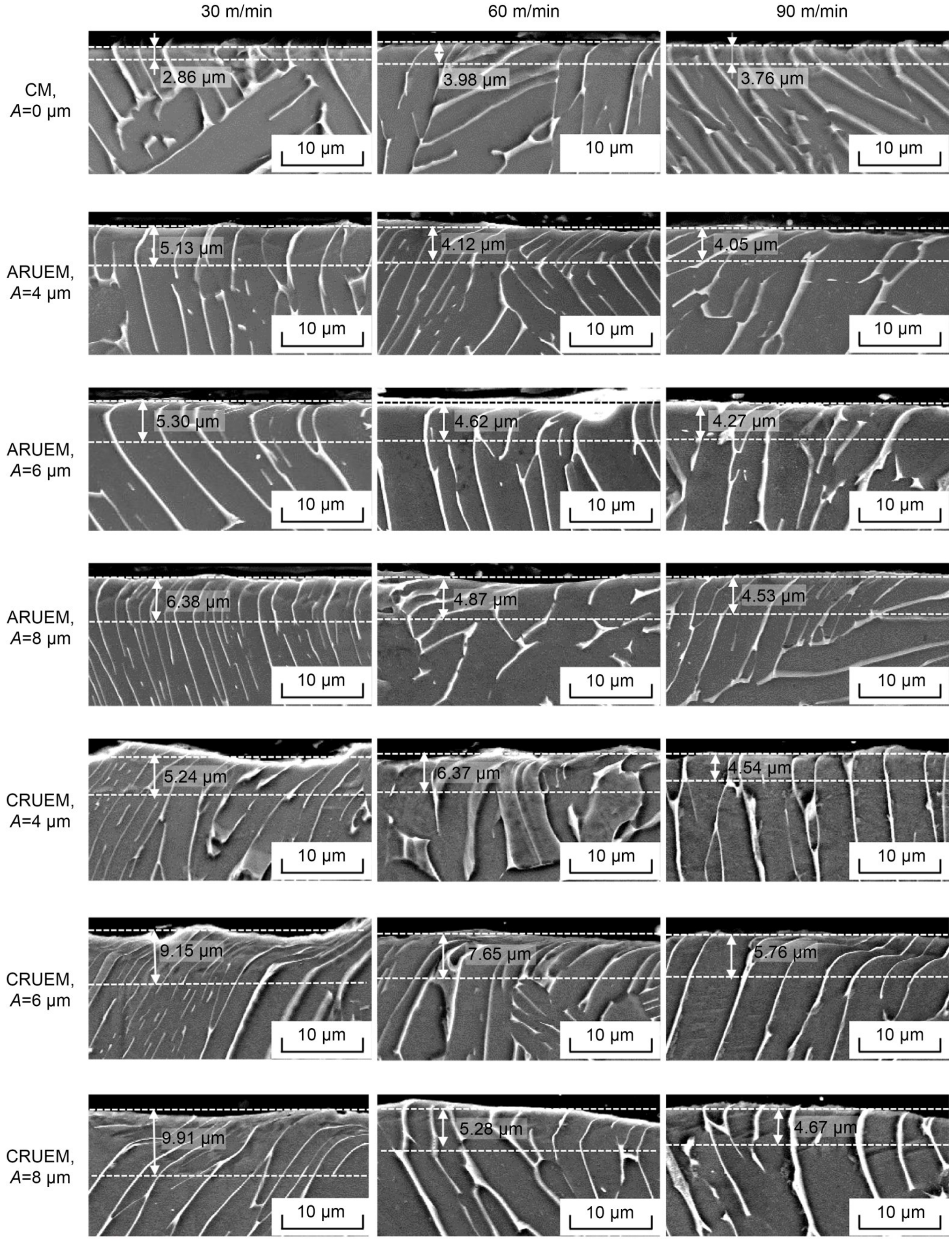

Fig. 13 Influence of elliptic vibration direction, vibration amplitude, and cutting speed on subsurface microstructure

speed directly affects the density of the ultrasonic impact and ironing action, with lower cutting speeds resulting in higher action densities.

As illustrated in Fig. 13, the plastic deformation layer thickness resulting from ARUEM continuously increased as the vibration amplitude increased. This phenomenon can be attributed to the increase in ironing force on the flank face of the cutting edges as the vibration amplitude rises. In CRUEM, the plastic deformation layer thickness initially increased and then decreased under higher vibration amplitudes at cutting speeds of 60 and 90 m/min, while it continuously increased when the speed was 30 m/min. This may be due to the increasing cutting ability of the cutting edges resulting from the rising cutting speed and vibrational force on the cutting edges, in turn leading to a decrease in the plastic deformation layer thickness. Sun et al. (2023) demonstrated that the accelerating effect of ultrasonic vibration-assisted drilling can effectively improve the removal rate of material.

Overall, when the cutting speed was 30 m/min, the plastic deformation layer thickness in ARUEM was 78.9%−122.6% higher than in CM at different vibration amplitudes, while the plastic deformation layer thickness in CRUEM was 82.9%–245.8% higher than in CM. The plastic deformation layers in ARUEM were thinner than in CRUEM, which is related to more effective plastic extrusion of the ridges during CRUEM.

4.2.2 Residual stress

In Fig. 14, the residual stresses parallel to the feed direction on the machined surfaces under different cutting parameters are illustrated for ARUEM and CRUEM. During cutting, the mechanical load causes compressive stress, while the thermal load is responsible for tensile stress (Sun and Guo, 2009; Wang et al., 2017). Because of the small feed rate during cutting, the mechanical load plays a major role, and therefore the residual stresses on the machined surface are all compressive, presenting negative values. It is well known that the compressive stress on a machined surface can improve the fatigue resistance of the workpiece (Yuan et al., 2015).

As shown in Fig. 14, the residual compressive stresses of the surface machined with CM decreased as the cutting speed rose from 30 to 60 m/min, and increased when the cutting speed exceeded 90 m/min. This is because the thermal load increases as the cutting speed increases, which leads to lower compressive stress, and the mechanical load increases substantially when the cutting speed exceeds 90 m/min, causing an increase in compressive stress (Liu et al., 2019b). The residual compressive stress upon the surfaces machined with ARUEM and CRUEM increased as the cutting speed decreased, owing to the increased ironing density of the tool flank on the workpiece at lower cutting speeds.

In ARUEM, the residual compressive stress was the highest at a vibration amplitude of 4 μm, then gradually decreased as the amplitude increased from 4 to 8 μm. The maximum growth ratio compared to CM was within the range of 19.0%−53.4%. As shown in Fig. 7, ironing occurs in the area that will be removed by the subsequent cutting process. However, the ironing effect in the removed area can affect the residual stress on the final machined surface. Because the distance

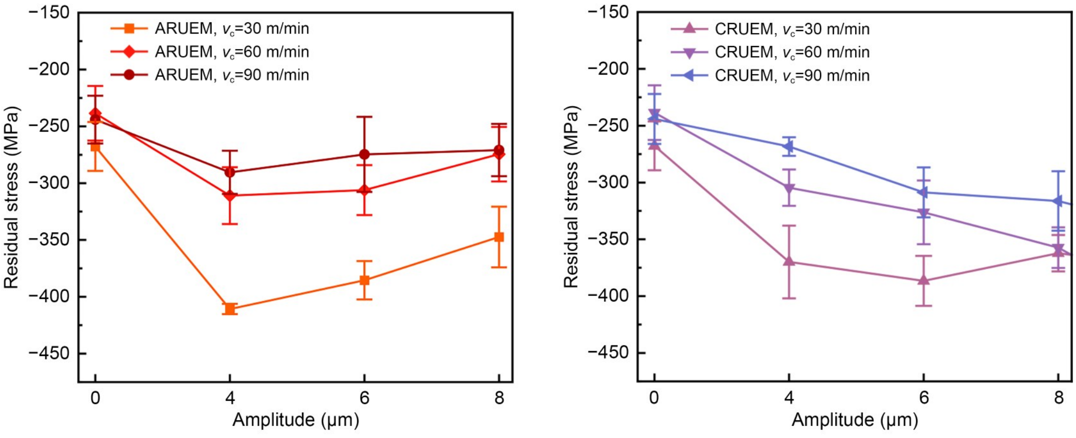

(a) (b)

Fig. 14 Influence of vibration amplitude and cutting speed on residual stress for: (a) ARUEM; (b) CRUEM

between the ironing area and the final surface is shorter at smaller vibration amplitudes, the residual compressive stresses of the machined surface are the highest at a vibration amplitude of 4 μm, and decrease as the amplitude continues to increase.

For CRUEM, as the vibration amplitude increased, the residual compressive stresses increased for cutting speeds of 60 and 90 m/min, with the maximum growth ratios (compared to CM) being 49.8% and 29.6%, respectively. However, at a cutting speed of 30 m/min, the residual compressive stresses were higher at vibration amplitudes of 4–6 μm, and decreased when the amplitude reached 8 μm. The maximum increase ratio was 44.4%. This can be attributed to more severe ploughing and ironing phenomena occurring at lower vibration amplitudes (Yang et al., 2020).

Overall, ARUEM can effectively improve the residual compressive stress compared to CM. Both ARUEM and CRUEM effectively enhanced the surface residual compressive stress, with the residual compressive stress under ARUEM being higher than under CRUEM at a vibration amplitude of 4 μm. This may be because the pressed ridges resulting from ARUEM are partially removed during subsequent cutting, yielding a final surface with a higher residual compressive stress.

4.2.3 Micro-hardness

Under the mechanical and thermal actions associated with cutting, deformation and refinement of the grains occur in the subsurface of the workpiece, which leads to improvement in the micro-hardness of the machined surface (Klumpp et al., 2018; Ren and Liu, 2018). An increase in micro-hardness can optimize the tribological properties of the machined surface, improving fatigue properties (Klumpp et al., 2018). The micro-hardness values of the surfaces machined using ARUEM and CRUEM are presented in Fig. 15. The micro-hardness resulting from CM increases as the cutting speed rises from 30 to 60 m/min, and decreases when the cutting speed reaches 90 m/min. This follows a similar trend to the plastic deformation layer thickness, since both quantities are influenced by mechanical and thermal properties during the cutting process.

The micro-hardness for both ARUEM and CRUEM increased as the vibration amplitude increased, demonstrating that the ultrasonic impact strength has a significant effect on the micro-hardness.

In ARUEM and CRUEM, the micro-hardness values at a cutting rate of 30 m/min are similar to those at 60 m/min, and both are significantly higher than those at 90 m/min. This phenomenon can be explained by the increase in ultrasonic ironing density (at 30 m/min) and the increase in cutting speed (at 60 m/min), both of which lead to plastic deformation and increased surface micro-hardness. However, in ARUEM, the micro-hardness increases significantly when the vibration amplitude reaches 8 μm, at a cutting speed of 30 m/min. The changes in surface micro-hardness and the thickness of the plastic deformation layer vary with cutting speed, a fact which is attributed to the differing sensitivities of these two indices to ultrasonic ironing density and cutting speed. The maximum micro-hardening rate under ARUEM was 19.3%, while under CRUEM it was 18.8%.

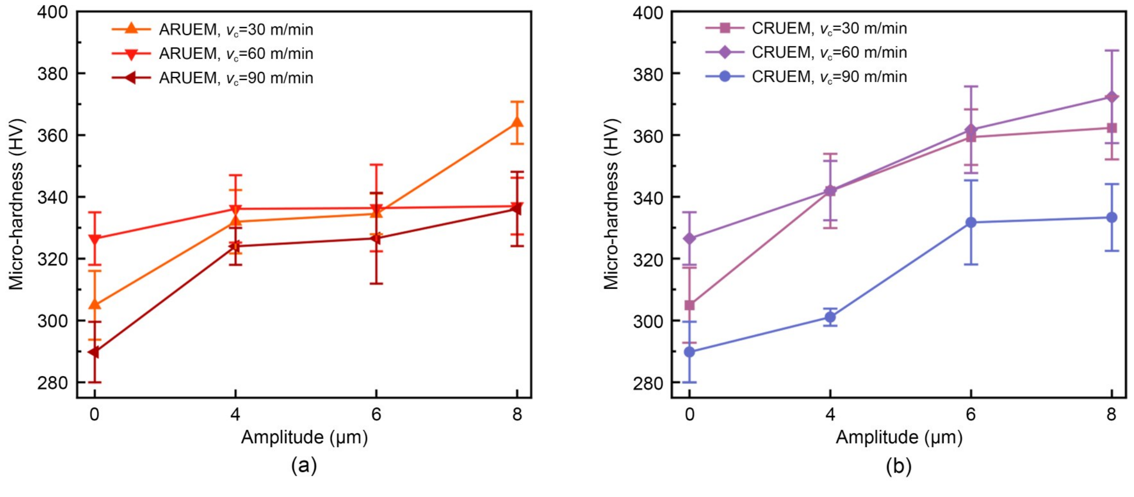

Fig. 15 Influence of vibration amplitude and cutting speed on micro-hardness of the machined surface for: (a) ARUEM; (b) CRUEM

5 Conclusions

A novel anticlockwise rotary ultrasonic elliptical machining (ARUEM) method was proposed to address the issue of high surface roughness in conventional clockwise rotary ultrasonic elliptical machining (CRUEM). The surface formation and subsurface strengthening mechanisms in ARUEM were systematically investigated, and compared to the results of CRUEM and conventional milling (CM).

The surface formation mechanism in ARUEM was revealed based on a corrected motion trajectory for the cutting edge. Moreover, it was found that a lower residual height of the machined surface could be obtained in ARUEM as compared to CRUEM.

The ARUEM-machined surface exhibited a uniform texture, reducing scratches and fluctuations compared to CM. The surface roughness R_a was up to 50% lower relative to CRUEM, and was accompanied by reduced ridge heights and undulations. This was primarily due to the lower residual height and the enhanced cutting ability of ARUEM.

Both ARUEM and CRUEM showcased notable strengthening effects compared to CM. For ARUEM, the maximum increases in plastic deformation layer thickness, surface residual compressive stress, and surface micro-hardness were 122.6%, 53.4%, and 19.3%, respectively. For CRUEM, the corresponding increases were 245.8%, 49.8%, and 18.8%. Although ARUEM resulted in a thinner plastic deformation layer, its associated surface residual compressive stress and microhardness were comparable to those of CRUEM.

ARUEM therefore shows promise for applications requiring enhanced surface strengthening and strict surface roughness control during machining, particularly those involving difficult-to-cut materials.

Acknowledgments

This work is supported by the National Natural Science Foundation of China (Nos. 91960203 and 52375399) and the Chinese Aeronautical Establishment Aeronautical Science Foundation (No. 2022Z045051001).

Author contributions

Deyuan ZHANG and Lianxing LIU designed the research. Lianxing LIU, Enze YING, and Zhefei SUN processed the corresponding data. Lianxing LIU wrote the first draft of the manuscript. Daxi GENG, Deyuan ZHANG, and Xinggang JIANG helped to organize the manuscript. Lianxing LIU and Daxi GENG revised and edited the final version.

Conflict of interest

Lianxing LIU, Xinggang JIANG, Enze YING, Zhefei SUN, Daxi GENG, and Deyuan ZHANG declare that they have no conflict of interest.

References

Brehl DE, Dow TA, 2008. Review of vibration-assisted machining. *Precision Engineering*, 32(3):153-172. https://doi.org/10.1016/j.precisioneng.2007.08.003

Cellier A, Chalon F, Grimal-Perrigouas V, et al., 2014. Effects of cutting angles in Ti-6Al-4V milling process on surface integrity: influence of roughness and residual stresses on fatigue limit. *Machining Science and Technology*, 18(4): 565-584. https://doi.org/10.1080/10910344.2014.955369

Chang BQ, Yi ZX, Zhang F, et al., 2024. A comprehensive research on wear resistance of GH4169 superalloy in longitudinal-torsional ultrasonic vibration side milling with tool wear and surface quality. *Chinese Journal of Aeronautics*, 37(4):556-573. https://doi.org/10.1016/j.cja.2023.07.009

Chen FY, Wang DZ, Wu SJ, 2021. Influence of ultrasonic vibration-assisted cutting on ploughing effect in cutting Ti6Al4V. *Archives of Civil and Mechanical Engineering*, 21(2):42. https://doi.org/10.1007/s43452-021-00196-5

Hu GF, Xin WD, Zhang M, et al., 2024. Developmental and experimental study on a double-excitation ultrasonic elliptical vibration-assisted cutting device. *Machines*, 12(6):379. https://doi.org/10.3390/machines12060379

Jiang XG, Wang KQ, Shao RJ, et al., 2018. Self-compensation theory and design of contactless energy transfer and vibration system for rotary ultrasonic machining. *IEEE Transactions on Power Electronics*, 33(10):8650-8660. https://doi.org/10.1109/Tpel.2017.2782702

Jiang YA, Pi J, Zhang YZ, et al., 2020. Research on the tool tip trajectory deflection control and cutting characteristics of elliptical vibration cutting based on guided wave transmission. *The International Journal of Advanced Manufacturing Technology*, 108(9-10):3101-3117. https://doi.org/10.1007/s00170-020-05552-y

Jiao ZH, Kang RK, Du DX, et al., 2023. Elliptical vibration cutting of large-size thin-walled curved surface parts of pure iron by using diamond tool with active cutting edge shift. *Chinese Journal of Aeronautics*, 36(6):402-419. https://doi.org/10.1016/j.cja.2022.08.015

Klumpp A, Maier S, Chen H, et al., 2018. Influence of work-hardening on fatigue crack growth, effective threshold and crack opening behavior in the nickel-based superalloy Inconel 718. *International Journal of Fatigue*, 116:257-267. https://doi.org/10.1016/j.ijfatigue.2018.06.033

Komatsu K, 1985. Constant vibration amplitude method of piezoelectric transducer using a PLL (phase locked loop). *Japanese Journal of Applied Physics*, 24(S1):159-162. https://doi.org/10.7567/JJAPS.24S1.159

la Monaca A, Murray JW, Liao ZR, et al., 2021. Surface integrity in metal machining–part II: functional performance.

International Journal of Machine Tools and Manufacture, 164:103718.
https://doi.org/10.1016/j.ijmachtools.2021.103718

Liao YS, Gui Y, Wang KJ, et al., 2021. Activation energy of calcium sulfoaluminate cement-based materials. *Materials and Structures*, 54(4):162.
https://doi.org/10.1617/s11527-021-01753-3

Liao ZR, Polyakov M, Diaz OG, et al., 2019. Grain refinement mechanism of nickel-based superalloy by severe plastic deformation–mechanical machining case. *Acta Materialia*, 180:2-14.
https://doi.org/10.1016/j.actamat.2019.08.059

Liao ZR, la Monaca A, Murray J, et al., 2021. Surface integrity in metal machining–part I: fundamentals of surface characteristics and formation mechanisms. *International Journal of Machine Tools and Manufacture*, 162:103687.
https://doi.org/10.1016/j.ijmachtools.2020.103687

Liu JJ, Jiang XG, Han X, et al., 2019a. Influence of parameter matching on performance of high-speed rotary ultrasonic elliptical vibration-assisted machining for side milling of titanium alloys. *The International Journal of Advanced Manufacturing Technology*, 101(5-8):1333-1348.
https://doi.org/10.1007/s00170-018-3006-6

Liu JJ, Jiang XG, Han X, et al., 2019b. Effects of rotary ultrasonic elliptical machining for side milling on the surface integrity of TI-6Al-4V. *The International Journal of Advanced Manufacturing Technology*, 101(5-8):1451-1465.
https://doi.org/10.1007/s00170-018-2847-3

Liu YH, Geng DX, Zhang DY, et al., 2023. Cutting performance and surface integrity for rotary ultrasonic elliptical milling of Inconel 718 with the ball end milling cutter. *Journal of Materials Processing Technology*, 319:118094.
https://doi.org/10.1016/j.jmatprotec.2023.118094

Ma CX, Shamoto E, Moriwaki T, et al., 2004. Study of machining accuracy in ultrasonic elliptical vibration cutting. *International Journal of Machine Tools and Manufacture*, 44(12-13):1305-1310.
https://doi.org/10.1016/j.ijmachtools.2004.04.014

Ma L, Xu GT, Wang G, et al., 2018. A new method for evaluating the influences of surface topography on fatigue propriety of the random machined surfaces. *MATEC Web of Conferences*, 165:22028.
https://doi.org/10.1051/matecconf/201816522028

Moriwaki T, Shamoto E, 1995. Ultrasonic elliptical vibration cutting. *CIRP Annals*, 44(1):31-34.
https://doi.org/10.1016/S0007-8506(07)62269-0

Niu Y, Jiao F, Zhao B, et al., 2017. Multiobjective optimization of processing parameters in longitudinal-torsion ultrasonic assisted milling of Ti-6Al-4V. *The International Journal of Advanced Manufacturing Technology*, 93(9-12): 4345-4356.
https://doi.org/10.1007/s00170-017-0871-3

Pang Y, Feng PF, Wang JJ, et al., 2021. Performance analysis of the longitudinal-torsional ultrasonic milling of Ti-6Al-4V. *The International Journal of Advanced Manufacturing Technology*, 113(5-6):1255-1266.
https://doi.org/10.1007/s00170-021-06682-7

Ren XP, Liu ZQ, 2018. Microstructure refinement and work hardening in a machined surface layer induced by turning Inconel 718 super alloy. *International Journal of Minerals, Metallurgy, and Materials*, 25(8):937-949.
https://doi.org/10.1007/s12613-018-1643-2

Seenath AA, Sarhan AAD, 2024. A state-of-the-art review on cutting tool materials and coatings in enhancing the tool performance in machining the superior nickel-based superalloys. *Arabian Journal for Science and Engineering*, 49(8):10203-10236.
https://doi.org/10.1007/s13369-024-08745-9

Shaikh VA, Scharf TW, Boubekri N, 2017. Microlubrication machining of 1018 steel: the effect of a biodegradable lubricant on the microstructural integrity. *Lubrication Science*, 29(6):357-376.
https://doi.org/10.1002/ls.1373

Shamoto E, Moriwaki T, 1999. Ultaprecision diamond cutting of hardened steel by applying elliptical vibration cutting. *CIRP Annals*, 48(1):441-444.
https://doi.org/10.1016/S0007-8506(07)63222-3

Sharma VS, Dogra M, Suri NM, 2009. Cooling techniques for improved productivity in turning. *International Journal of Machine Tools and Manufacture*, 49(6):435-453.
https://doi.org/10.1016/j.ijmachtools.2008.12.010

Stopka KS, Yaghoobi M, Allison JE, et al., 2021. Effects of boundary conditions on microstructure-sensitive fatigue crystal plasticity analysis. *Integrating Materials and Manufacturing Innovation*, 10(3):393-412.
https://doi.org/10.1007/s40192-021-00219-2

Stopka KS, Yaghoobi M, Allison JE, et al., 2023. Microstructure-sensitive modeling of surface roughness and notch effects on extreme value fatigue response. *International Journal of Fatigue*, 166:107295.
https://doi.org/10.1016/j.ijfatigue.2022.107295

Sui H, Zhang XY, Zhang DY, et al., 2017. Feasibility study of high-speed ultrasonic vibration cutting titanium alloy. *Journal of Materials Processing Technology*, 247:111-120.
https://doi.org/10.1016/j.jmatprotec.2017.03.017

Sun J, Guo YB, 2009. A comprehensive experimental study on surface integrity by end milling Ti–6Al–4V. *Journal of Materials Processing Technology*, 209(8):4036-4042.
https://doi.org/10.1016/j.jmatprotec.2008.09.022

Sun LJ, Zheng K, Liao WH, 2022. Chatter suppression and stability analysis of rotary ultrasonic milling titanium alloy thin-walled workpiece. *The International Journal of Advanced Manufacturing Technology*, 118(7-8):2193-2204.
https://doi.org/10.1007/s00170-021-07658-3

Sun ZF, Geng DX, Meng FX, et al., 2023. High performance drilling of T800 CFRP composites by combining ultrasonic vibration and optimized drill structure. *Ultrasonics*, 134: 107097.
https://doi.org/10.1016/j.ultras.2023.107097

Sun ZF, Geng DX, Guo HL, et al., 2024. Introducing transversal vibration in twist drilling: material removal mechanisms and surface integrity. *Journal of Materials Processing Technology*, 325:118296.
https://doi.org/10.1016/j.jmatprotec.2024.118296

Ulutan D, Ozel T, 2011. Machining induced surface integrity in titanium and nickel alloys: a review. *International Journal*

of Machine Tools and Manufacture, 51(3):250-280.
https://doi.org/10.1016/j.ijmachtools.2010.11.003

Wang B, Liu ZQ, 2018. Influences of tool structure, tool material and tool wear on machined surface integrity during turning and milling of titanium and nickel alloys: a review. *The International Journal of Advanced Manufacturing Technology*, 98(5-8):1925-1975.
https://doi.org/10.1007/s00170-018-2314-1

Wang JT, Zhang DH, Wu BH, et al., 2017. Numerical and empirical modelling of machining-induced residual stresses in ball end milling of Inconel 718. *Procedia CIRP*, 58:7-12.
https://doi.org/10.1016/j.procir.2017.03.177

Wojciechowski S, Matuszak M, Powałka B, et al., 2019. Prediction of cutting forces during micro end milling considering chip thickness accumulation. *International Journal of Machine Tools and Manufacture*, 147:103466.
https://doi.org/10.1016/j.ijmachtools.2019.103466

Wu CJ, Chen SJ, Xiao CW, et al., 2019. Longitudinal–torsional ultrasonic vibration-assisted side milling process. *Proceedings of the Institution of Mechanical Engineers, Part C: Journal of Mechanical Engineering Science*, 233(10): 3356-3363.
https://doi.org/10.1177/0954406218819023

Xiao M, Wang QM, Sato K, et al., 2006. The effect of tool geometry on regenerative instability in ultrasonic vibration cutting. *International Journal of Machine Tools and Manufacture*, 46(5):492-499.
https://doi.org/10.1016/j.ijmachtools.2005.07.002

Yang ZC, Zhu LD, Zhang GX, et al., 2020. Review of ultrasonic vibration-assisted machining in advanced materials. *International Journal of Machine Tools and Manufacture*, 156: 103594.
https://doi.org/10.1016/j.ijmachtools.2020.103594

Yao J, Li X, Du BR, et al., 2024. Research status of influence mechanism of surface integrity on fatigue behavior of metal workpieces: a review. *The International Journal of Advanced Manufacturing Technology*, 131(7-8):3401-3419.
https://doi.org/10.1007/s00170-024-13195-6

Yuan X, Yue ZF, Wen SF, et al., 2015. Numerical and experimental investigation of the cold expansion process with split sleeve in titanium alloy TC4. *International Journal of Fatigue*, 77:78-85.
https://doi.org/10.1016/j.ijfatigue.2015.03.014

Zhang JG, Cui T, Ge C, et al., 2016. Review of micro/nano machining by utilizing elliptical vibration cutting. *International Journal of Machine Tools and Manufacture*, 106: 109-126.
https://doi.org/10.1016/j.ijmachtools.2016.04.008

Zhang YM, Wang XB, Wu XF, et al., 2023. Stability analysis and chatter suppression of ultrasonic elliptical vibration milling of Ti-6Al-4V alloy. *The International Journal of Advanced Manufacturing Technology*, 129(3-4):1301-1314.
https://doi.org/10.1007/s00170-023-12341-w

Electronic supplementary materials

Sections S1–S8